Advanced Energy and Sustainability Research

ADVANCED ENERGY & SUSTAINABILITY RESEARCH Open Access

www.advenergysustres.com

RESEARCH ARTICLE OPEN ACCESS

Generating Power Through Salinity Gradients in Osmotic Engines via Microfluidic Synthesized Hydrogel Particles

Huan Zhang | Sarah Palloks | Jan Schmid | Michael Pollard | Xiaohe Xu | Manfred Wilhelm

Institute for Chemical Technology and Polymer Chemistry (ITCP), Karlsruhe Institute of Technology (KIT), Karlsruhe, Germany

Correspondence: Manfred Wilhelm (manfred.wilhelm@kit.edu)

Received: 10 March 2026 | **Revised:** 18 April 2026 | **Accepted:** 24 April 2026

Keywords: microfluidic synthesis | osmotic engine | polyelectrolyte hydrogel | renewable energy | salinity gradient

ABSTRACT

Salinity-gradient energy at river deltas represents a promising yet underexploited renewable resource. Osmotic engines can harvest this energy by converting chemical potential differences between fresh and saline water into mechanical power. Hydrogels are potential osmotic matrix materials due to their high water-uptake capacity, salt-responsive swelling, and mechanical resilience. Cyclic swelling in fresh water and deswelling in saline water of hydrogels drives piston motion in the osmotic engine, enabling mechanical energy generation. In this work, monodisperse hydrogel particles are synthesized via a microfluidic device and the effects of key synthesis parameters on hydrogel properties are investigated. Two osmotic engines with different volumes and height-to-diameter ratios are designed and evaluated, with operating parameters including gel mass, cycle time, applied pressure, and flow rate optimized to maximize power output. The maximum power of 13.20 W per 1 kg dry hydrogel is achieved with deionized water and NaCl solution of 43 $g \cdot L^{-1}$ using poly(acrylic acid) hydrogels with a diameter of 233 μm and a degree of crosslinking of 0.5 mol%. These results highlight the potential of microfluidic-synthesized hydrogel particles as osmotic matrix materials and demonstrate that rational engine design and operating parameter optimization significantly enhance the performance of energy conversion from salinity gradients.

1 | Introduction

It is estimated that worldwide energy consumption will increase by 48% between 2012 and 2040, driven substantially by a projected 29% rise in population and further improvements in average living standards [1–3]. The consumption of traditional energy resources like coal, oil, or gas amounts to around 500 EJ in 2023, accounting for over 80% of total primary energy consumption [4]. This results in harmful gas emissions, including greenhouse gases (especially CO_2 and CH_4), and causes climate change, making fossil fuels unsuitable for sustainable utilization. Therefore, transitioning to sustainable, low-emission alternative energy sources is an urgent issue [5, 6]. Seawater is one of the most abundant natural resources which covers 71% of the surface area on the earth. In river delta areas, fresh water mixes with seawater, and the salinity difference between them corresponds to a theoretical osmotic pressure of about 25 atm, which represents the potential energy stored in the gradients [7–9]. Extracting energy from such gradients has been a research topic since the last century [10–13]. Based on the osmotic pressure difference, it is estimated that approximately 0.70–0.75 kWh of energy can be generated through 1 m^3 of freshwater flowing into the ocean [14]. This process is fundamentally the reverse of seawater desalination. In practice, however, desalination requires 2.5–4.0 kWh per cubic meter, which is still considerably high due to the limited efficiency of current desalination technologies [15]. Furthermore, the potential of global osmotic power generation is estimated to be 2.6 TW [16], corresponding to around 82 EJ per year, which could potentially replace around 16% of global energy consumption from conventional sources [17, 18]. Therefore, salinity gradients could be a promising energy source, as they would not cause pollution and are not dependent on

rather fast, daily changing weather conditions affecting solar or wind energy production. The widely used technologies to extract this energy are reverse electrodialysis (RED) and pressure retarded osmosis (PRO), which are operated with membranes [7]. However, preventive treatment and regular cleaning of the membranes are necessary and costly due to the biofouling and scaling. Lin et al. critically evaluated that PRO and RED are unlikely to become economically viable due to their inherently low power density, high membrane cost, and system-level complexity [19]. In contrast to membrane-based systems, polyelectrolyte hydrogels are considered more suitable for harvesting salinity-gradient energy due to their low material cost (e.g., 2 €/kg dry hydrogel, year 2026), structural simplicity, scalability, and lower susceptibility to biofouling, which has drawn increasing research attention [20–24].

Polyelectrolyte hydrogels, which are also called superabsorbent polymers (SAPs), are three-dimensional polymer networks containing a large amount of charged, hydrophilic groups. These charged network systems typically show high (up to a factor of 1000) and fast (within seconds) water absorbency [25–27]. Another outstanding feature of SAPs is that their general swelling behavior is highly responsive to ionic concentration [28, 29]. Additionally, SAPs have a quite high tolerance to internal stress and volume compression. For example, it has been reported that hydrogel-based actuators are capable of producing stress outputs on the order of 1 MPa (equivalent to ca. 10 bar pressure) [29]. Because of the unique combination of high water absorbency, ion-responsive swelling and mechanical resilience, SAPs are extensively used in diapers [30, 31], tissue engineering, drug delivery, sensors, and actuators [32, 33], and could also be applied in salt gradient power generation. To describe the swelling behavior of elastomeric networks, Flory and Rehner developed a theoretical framework based on the change in free energy accompanying network swelling. In this model, the total free energy is expressed as the sum of distinct thermodynamic contributions, including the polymer-solvent mixing free energy and the elastic deformation of the polymer network [34, 35]. This framework was subsequently extended to polyelectrolyte gels by incorporating an ionic osmotic pressure term that accounts for the Donnan equilibrium between the gel and the surrounding solution [28]. Building upon this extended formulation, numerous studies have been devoted to the volumetric response kinetics of charged hydrogels to salinity gradients [17, 22, 36].

As already mentioned, SAPs exhibit a salt concentration-dependent swelling response: they swell to a larger extent in freshwater due to electrostatic repulsions between the charged polymer chains, whereas in saline water they swell less due to the shielded electrostatic repulsion [17]. An osmotic engine can be designed to take advantage of this variable response by moving a weight on a piston upward during expansion caused by fresh water to produce power, followed by downward movement of the piston during contraction via saline water to complete a cycle. Syringe-type engines have been utilized as they can work simply by making several holes on the piston, so that the liquid can be flushed in from the inlet through the SAPs and the surplus can be extracted via the holes [37, 38]. However, due to a large height-to-diameter ratio of the syringe, SAPs will stack to a certain height and the swelling of the first layer may fill the voids between particles, which blocks flow to the inner layers and causes so-called gel-blocking that will substantially reduce the speed of the motion [39]. There are two possible ways to reduce gel-blocking. The first one is to reduce the height-to-diameter ratio of the engine, thereby decreasing the stacking and squeezing between SAP layers [40]. Following this strategy, we redesigned the engine with two additional considerations: (a) high mechanical strength to push large weights on the piston without collapsing, and (b) separate inlets for freshwater and saline to shorten liquid residence time and improve flushing efficiency. The second approach is to employ spherically shaped polyelectrolyte hydrogels. Due to the likelihood of the face-centered cubic (fcc) packing of the resulting spheres, a close packing of spheres maintains a high amount of connected interstitial voids, which reaches up to 26% by volume in an ideal case [41]. This simplified value is only valid if no further deformation of the spheres is assumed, e.g., at high degrees of crosslinking (DC). By increasing the space between the spheres, liquid transportation during expansion and shrinkage is improved. The microfluidic technique is a well-known way to fabricate such monodisperse spherical droplets through coflowing two immiscible fluids in capillaries to induce droplet formation [42]. The droplet size can be controlled by the flow rate of the two fluids and the diameter of the capillaries during synthesis.

Hydrogels based on poly(acrylic acid) (PAA) are a type of SAP that can absorb up to hundreds of times its own weight in water due to its high charge density after chemical neutralization of the carboxylic acid groups (—COOH) into negatively charged carboxylate groups ($—COO^-$) [30, 43]. Therefore, PAA could be a promising material to produce mechanical power by switching between deionized (DI) water and a monovalent ion salt solution. This idea was explored first in 2014 by Zhu et al. [20], who reported an energy extraction from PAA hydrogels by adding weights on the top, and obtained an energy output of $0.12\ W{\cdot}kg^{-1}$ of dry SAPs [20]. Since then, many studies have been carried out on the generation of osmotic energy by PAA. In 2017, Arens et al. found a maximum mean power output of $0.23\ W{\cdot}kg^{-1}$ with ground PAA particles with irregular shapes having a DC of 1.7 mol % and particle sizes between 370 and 670 µm [40]. In 2021, Bui and co-workers synthesized a semi-interpenetrating hydrogel of PAA, which produced up to $3.7\ W{\cdot}kg^{-1}$ at optimum conditions [23]. In 2022, Hong et al. fabricated robust and antifouling poly(acrylic acid-co-acrylamide) hydrogels and obtained an output power of $1.72\ W{\cdot}kg^{-1}$ with different concentrations of NaCl solution [44].

In this work, two types of osmotic engines with different volumes and height-to-diameter ratios were designed and operated with spherical particles of partially neutralized PAA hydrogels which were synthesized through a microfluidic device. The differences in absorbency and mechanical behavior of PAA hydrogels with variable DC were explored first, and then the power generation of hydrogel particles of different diameters in two engines was compared. Last, the parameters for the operation of the engines were optimized with the goal to obtain maximum power output per unit mass of SAP.

2 | Results and Discussion

2.1 | Hydrogel Particle Synthesis via Microfluidics

Microfluidics is a technology that utilizes micrometer-scale channels to manipulate small amounts of fluid [45–48]. Microparticles prepared by microfluidic synthesis exhibit controllable sizes, highly uniform spherical shapes, and reduced cross-contamination [49–51]. A droplet-based microfluidic technique is employed here to generate monodisperse spherical hydrogel particles. The system uses a self-made flow-focusing glass capillary microfluidic device, as shown in Figure 1a. Its design and fabrication are described in Section 4.2. The flow rates of the oil and water phases and the diameters of the capillaries determine the size of resulting particles. During the operation, the water phase, which contains reactive components (e.g., monomer, crosslinker, and initiator), and the oil phase are both pumped into the capillaries and droplets of the water phase are formed at the intersection by the flow focusing of the oil phase. In this study, hydrogel particles with diameters of $D = 233$ and $D = 638$ µm after drying (abbreviated D233 and D638) were produced using different combinations of capillary tube sizes and flow rates. The synthesis parameters of the two particle types are listed in Table 1. Figure 1b,c display the optical microscope pictures of D233 and D638 after polymerization under UV light for 2 h and after vacuum drying. They confirm the spherical shape and narrow size distribution of the hydrogels (dry particle diameters of 638 ± 59 µm and 233 ± 30 µm) made via microfluidic device compared to a commercial SAP from BASF, which is listed as SAP Polyacrylate Sample 3 (Figure 1d).

While it is generally expected that smaller particles may exhibit faster swelling kinetics due to shorter diffusion pathways, further reduction of particle size was not pursued in the present work due to practical limitations of the specific microfluidic device. Generating smaller particles requires narrower capillary tubes and slower flow rates, which can lead to an early gelation of the pre-gel solution. In addition, elevated internal pressure in such confined geometries can lead to reduced uniformity in particle size distribution. These factors make the reliable and scalable production of smaller hydrogel particles challenging under the current setup. Therefore, a systematic investigation across a broader size range is proposed for future work, where alternative synthesis methods such as suspension polymerization could enable both smaller particle sizes and larger-scale production.

2.2 | Design and Working Principle of Osmotic Engines

The principle of power generation with an osmotic engine is shown in Figure 2a. After reaching equilibrium swelling in saline solution ($43\ g \cdot L^{-1}$ NaCl solution in this work, which results in a similar ionic strength as seawater [39]), the hydrogel particles are transferred into the engine. Then DI water, as a model for fresh water, is fed with a constant volume flux into the engine, resulting in a volume expansion of the hydrogel particles and thus the lifting of the weights on the piston which consequently produces mechanical power. To complete a swelling-shrinking cycle, in the next step saline water is fed into the engine, leading to a deswelling of the hydrogel particles and a return of the piston to the starting position. Both solutions are injected into the engine from the bottom and excess liquid is removed from the holes on the piston, so that the hydrogels can be immersed completely. The mass normalized mean output power can be calculated via Equation (1):

$$\overline{P} = \frac{m_{\text{weights}} * g * \Delta h}{\Delta t * m_{\text{gel}}} \tag{1}$$

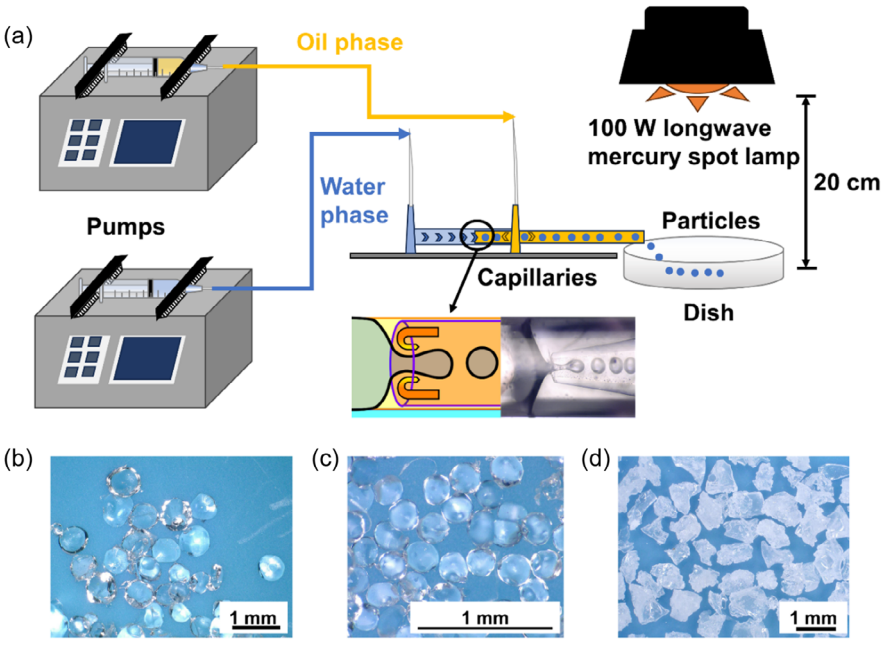

FIGURE 1 | (a) Illustration of the microfluidic setup used for hydrogel particle synthesis, employing a self-built flow-focusing glass capillary device. The droplets of the water phase are formed at the intersection by the flow focusing of the oil phase. (b) Spherical hydrogel particles of D638 made through microfluidic device after vacuum drying. (c) Spherical hydrogel particles of D233 made through microfluidic device after vacuum drying. (d) Commercial hydrogels from BASF, named SAP Polyacrylate Sample 3.

TABLE 1 | Particle diameters with varied sizes of the capillary tubes and applied flow rates.

Square channel width for water phase (mm)	Round channel diameter for oil phase (mm)	Flow rate of oil phase ($mL \cdot h^{-1}$)	Flow rate of water phase ($mL \cdot h^{-1}$)	Mean diameter ± standard deviation (μm)	Production rate of dried particles ($g \cdot h^{-1}$)
2.2	1.4	60	17	638 ± 59 (D638)	3
1.1	0.58	20	5.6	233 ± 30 (D233)	1

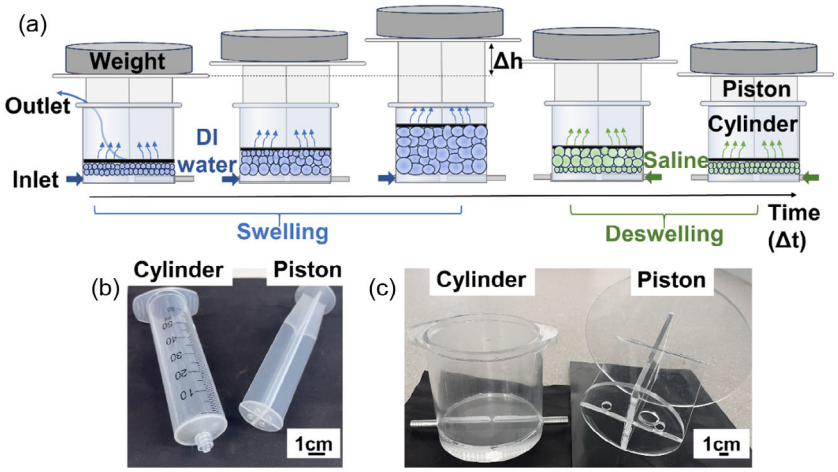

FIGURE 2 | (a) Principle of power generation through a salinity gradient with an osmotic engine. The hydrogels are constrained in a fixed cylinder and the movement of the weight is driven by hydrogel expansion in deionized water and shrinkage in saline water. (b) Photograph of engine 1.0 (syringe-type engine with a volume of 50 mL). (c) Photograph of engine 2.0 (volume of 1 L).

where $\overline{P}$ is the mean power normalized to the dry hydrogel mass as quantified over one complete cycle ($W \cdot kg^{-1}$), $m_{weights}$ is the mass of added weights (kg), g is the gravitational constant (9.81 $m\,s^{-2}$), Δh is the height change in the engine (m), Δt is the cycle time (s), and m_{gel} is the mass of dry gel (kg).

The NaCl solution was used as a simple model system instead of real seawater in this study. This choice is related to the chemical nature of the PAA hydrogel employed. PAA was selected in this work for several reasons: (1) It exhibits high swelling capacity in monovalent salt solutions due to the high charge density after pH neutralization. (2) AA has a simple chemical structure that facilitates free radical polymerization. (3) PAA-based SAPs are widely available as commercial products. However, the PAA hydrogel is an anionic polyelectrolyte containing abundant -COOH groups, which will interact irreversibly with divalent cations (e.g., Ca^{2+} and Mg^{2+}) in seawater. Such interactions promote interchain ionic bridging and chain aggregation, thereby reducing the swelling capacity of the hydrogel network. The NaCl solution was therefore used to avoid the multivalent ion effects. Future work could focus on developing alternative hydrogel systems, such as cationic poly(acrylamide-co-(3-acrylamidopropyl) trimethylammonium chloride) hydrogels, which have been reported by our group and are more compatible with complex ionic environments, including seawater [52]. In this work, engine 1.0, a simple syringe-type engine with a volume of 50 mL (diameter of 3 cm), was first used to test the mean output power of the synthesized hydrogels, as shown in Figure 2b. As there is only one inlet for the syringe at the bottom, the feeding tube needs to be manually transferred from DI water into saline after swelling and from saline to DI water after deswelling. To reduce the complexity of operation, improve the performance and scale up the experiment, engine 2.0 with a volume of 1 L and two inlets for fresh and salt water was designed, as shown in Figure 2c. One structural advantage of engine 2.0 is the lower mass-to-surface ratio due to the larger surface area (diameter of 10 cm), which leads to less height stacking, decreases squeezing between SAP layers, and reduces the friction between SAPs and the engine wall, thus reducing gel-blocking. For example, in engine 1.0, a dry mass of 0.2 g of hydrogels was used, corresponding to a dry mass-to-surface ratio of 283 $g \cdot m^{-2}$. In engine 2.0, an optimum dry mass of 1.5 g was investigated, yielding a dry mass-to-surface ratio of 191 $g \cdot m^{-2}$, which is lower than that in engine 1.0. The material used to build engine 2.0 is polymethyl methacrylate ("Plexiglas"), and this material, with a wall thickness of 5 mm, is sufficient to withstand the applied pressure up to 55 kPa (ca. 0.55 bar). Additionally, this transparent material is beneficial for observing the swelling of the hydrogels inside the engine during operation.

2.3 | Influence of Degree of Crosslinking on Absorbency and Mechanical Properties

To compare the influence of DC on absorbency and mechanical properties, D638 particles with DC ranging from 0.1 to 2.0 mol% were synthesized. The degree of neutralization (DN) was kept at 75 mol%, which has been experimentally confirmed to be close to the optimal value in a former publication [40]. According to Equation (1), the power output significantly depends on the height change in the engine of the hydrogels, the load on the piston and the diffusion time. The maximum height change is determined by the ratio of absorbency (Q) between saline and

DI water. The applied load is related to the effective Young's modulus (E) of the hydrogel particles under the respective solution conditions. Although E does not directly represent mechanical strength, within the same hydrogel system a higher modulus generally allows higher load-bearing capacity. Since all hydrogel particles tested here have identical dimensions (D638), variations in diffusion time arising from size differences are eliminated. As the analysis focuses on equilibrium modulus and absorbency, diffusion time is not considered. In this way, a figure of merit is defined as the difference of the product of absorbency and Young's modulus of the hydrogels between DI water and saline. This parameter can be used to predict the optimum DC value for power production in the osmotic engines.

The mechanical behavior of hydrogels was evaluated by small-amplitude oscillatory shear (SAOS) measurements. Once the shear modulus G was obtained, the corresponding E was calculated using the linear relationship between E and G, as shown in Equation (2) [53]:

$$G = \frac{E}{2 \times (1+\mu)} \tag{2}$$

where G is shear modulus, E is Young's modulus, and μ is Poisson's ratio. For isotropic materials of constant volume $\mu = 0.5$ is assumed, and as a result, $E = 3G$.

As the hydrogels are mostly elastic, the storage modulus (G') is considered to be representative for the G-module of the sample ($\tan\delta \approx 0.1$). The G' values of the hydrogel particles with varied DC were obtained through frequency sweeps under a constant pressure of 4 kPa and a constant strain amplitude of $\gamma_0 = 0.1\%$. The details of rheological measurements are shown in Section 4.4. The samples were immersed in saline and DI water separately until reaching equilibrium and then transferred to the rheometer. The resulting moduli are denoted as G'_S and G'_{DI}, respectively, as shown in Figure 3a,b. It is noticed that the storage modulus did not display a large dependency on angular frequency, and therefore G' at an angular frequency of $\omega = 1\ \text{rad}\cdot\text{s}^{-1}$ was selected for comparison. As expected, the moduli are increasing in both DI water and saline for fully swollen samples with increasing DC. This is because hydrogels with higher DC form polymer networks with more and shorter chain segments between crosslinks. The resulting higher density of elastically active chains per unit volume leads to an increased elastic modulus. For polymer networks, the shear modulus scales as $G \sim 1/M_e$, where M_e is the molecular weight between crosslinks, as originally derived for non-charged homopolymer melts [54, 55]. Although hydrogel particles exhibit substantially higher swelling in DI water than in saline, the observed difference in the swollen-state storage modulus is small. This may be because under SAOS measurements, the soft and highly swollen particles in DI water deform more easily and establish larger contact areas with the geometry, which can lead to an increase in the measured modulus [56, 57]. It should be noticed that the G' values obtained here may underestimate the true bulk storage modulus, as the hydrogel particles do not fully occupy the measurement geometry, resulting in a spatially inhomogeneous stress distribution. Nevertheless, comparisons of relative moduli obtained under consistent testing conditions can still provide useful insights and predict trends in output power production for the osmotic engines.

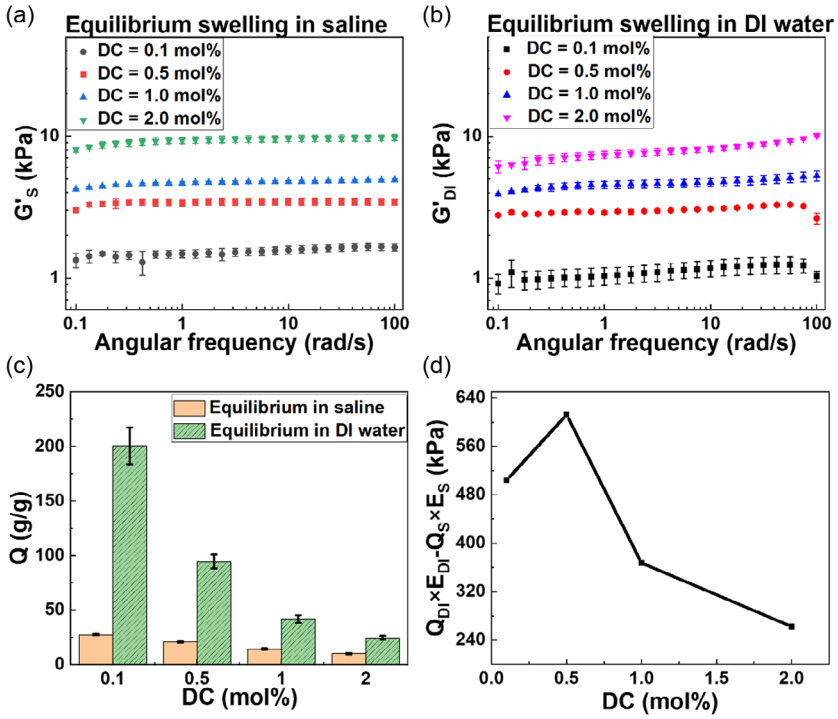

FIGURE 3 | (a) Storage moduli G' of D638 particles with varied DC at equilibrium swelling in saline. (b) Storage moduli G' of D638 particles with varied DC at equilibrium swelling in DI water. (c) Absorbency Q of D638 particles with varied DC swelling equilibrium in saline and DI water. (d) Difference of the products of absorbency and Young's modulus after equilibrium swelling in DI water and saline with varied DC of D638 particles ($Q_{DI} \times E_{DI} - Q_S \times E_S$, kPa), which is used as a figure of merit to predict the optimum DC for power output. Error bars represent standard deviation from three independent experiments ($n = 3$).

The absorbency of the hydrogel particles quantifies the amount of solution absorbed per gram of dry hydrogel. It depends strongly on the salt content of the aqueous solution. With increasing salt concentration, the difference in the osmotic pressure between hydrogel and external solution is reduced, thereby lowering the thermodynamic driving force for swelling [52]. The Q values with varied DC were measured after reaching equilibrium swelling in saline and DI water, as shown in Figure 3c. The calculations are shown in Equations (3) and (4):

$$Q_S = \frac{m_S - m_{dry}}{m_{dry}} \tag{3}$$

$$Q_{DI} = \frac{m_{DI} - m_{dry}}{m_{dry}} \tag{4}$$

where Q_S is the equilibrium absorbency of the hydrogels in saline, m_S is the mass of the hydrogels after swelling to equilibrium in saline solution, m_{dry} is the dry mass of the hydrogels, Q_{DI} is the equilibrium absorbency of the hydrogels in DI water, and m_{DI} is the mass of the hydrogels after swelling to equilibrium in DI water.

With increasing DC, both Q_S and Q_{DI} decrease as already mentioned, due to denser polymer networks with shorter chain segments between crosslinks. For hydrogel particles with a DC of 0.1 mol%, Q_{DI} is around 10 times higher than Q_S, but this ratio decreases with higher DC (Table S1). This can be explained by the interplay between ionic and elastic contributions to the swelling pressure. At low DC, the ionic osmotic pressure dominates the swelling behavior, while with increasing DC, the elastic counterforce to swelling becomes more significant, diminishing the relative contribution of the ionic osmotic pressure, and thus reducing the difference between Q_{DI} and Q_S. As a higher ratio means more height change between DI water and saline and thus higher output power, lower DC values are beneficial for power generation in osmotic engines. On the other hand, hydrogels with lower Young's modulus correspond to lower maximum loads on the top, reducing the achievable power output of the engine. Consequently, there is a need to search for the optimum conditions. The difference of the product of E and Q in DI water and saline solution ($Q_{DI} \times E_{DI} - Q_S \times E_S$, kPa) is used as a figure of merit to predict the power production potential of hydrogel particles with varied DC, as mentioned above. The results are presented in Figure 3d and more details are listed in Table S1. From the proposed figure of merit, it is predicted that the hydrogel particles with DC = 0.5 mol % have the potential to produce the maximum power. The equilibrium absorbency and Young's modulus were used here to provide intrinsic and limiting material properties rather than to simulate operational dynamics. All samples were tested under identical conditions at the same final state, ensuring reliable comparisons and material selection under practical application conditions. The power output measurements under realistic osmotic engine operating conditions are presented in Section 2.4 and 2.5.

2.4 | Power Generation via Engine 1.0

The influence of DC and particle diameters on power generation was explored in engine 1.0. Particles of D638 with varied DC were tested first. The engine was operated at a fixed dry hydrogel mass of 0.2 g and a liquid flow rate of 10 mL·min^{-1}. During the actual power-generation process, hydrogels will deform under pressure (which additionally causes gel-blocking) and the deformation helps the gels to withstand more stress for several reasons: (1) It leads to stress redistribution over a larger area and thus avoids fracture. (2) Hydrogels may exhibit nonlinear strain-stiffening behavior due to the stretching and alignment of polymer chains or network segments under increasing deformation. As compression proceeds, the effective stiffness of the hydrogel increases, which can suppress further localized deformation and prevents structural collapse. (3) The breaking of hydrogen bonds and ionic associations during deformation leads to network rearrangement, which dissipates mechanical energy and prevents sudden failure in hydrogels [58, 59]. To produce detectable deformation for hydrogels with different DC and enable meaningful power comparison, a constant external pressure of 28 kPa (applied via a weight of 2 kg in engine 1.0 with a surface area of 7.07 cm^2) was used across all samples. Under the fixed applied pressure, the influence of DC on power output is directly reflected in the height change. From Figure 4a, we observe that all the hydrogel particles can endure three consecutive swelling-shrinking cycles under a pressure of 28 kPa and this confirms that the particles do not break macroscopically under this stress. Additionally, it can be seen that the height change of the piston during operation increases with decreasing DC, which is beneficial for power production. As shown in Figure 4b, the maximum output power of 1.49 W·kg^{-1} is obtained from particles with a DC of 0.1 mol%. This DC value is lower than the optimum DC predicted by the figure of merit (see Figure 3d). The deviation could be explained by the high swelling factor of particles with DC = 0.1 mol% and their intact structures in the initial cycle. However, it can be observed that in subsequent cycles the power is decreasing. There are two possible reasons for the decrease: (1) Some particles are macroscopically fractured due to the poor mechanical strength, which leads to more gel-blocking and thus a retarded expansion after flooding the engine with DI water again. (2) The sol is washed away which decreases the charge density. The first argument is supported by the optical microscope pictures after 10 consecutive swelling-shrinking cycles in engine 1.0 under a pressure of 28 kPa, as shown in Figure S1. Through the comparison of particles swelling with or without pressure, we found that hydrogels with a DC of 0.5 mol% can keep the spherical shapes under 28 kPa, whereas with DC of 0.1 mol% the particles are partly broken under the same pressure. In this way hydrogels of DC = 0.1 mol% are not suitable for long-term application under 28 kPa. In contrast, particles with DC values of 0.5, 1.0, 2.0 mol% show an increase in output power in consecutive cycles. This may be caused by the progressive rearrangement of the polymer network, which might gradually evolve over repeated cycles, leading to a looser crosslinked structure and thus the observed increase in power output [60]. In conclusion, the DC value of 0.5 mol% is chosen as the optimum parameter under the tested conditions, which is consistent with the prediction from the difference of the products of absorbency and Young's modulus after swelling in DI water and saline (Figure 3d), confirming the reliability of the prediction. This DC value was further used in synthesizing hydrogel particles of a different, smaller diameter (D233).

Through the comparison of the output power of hydrogel particles with the same DC (0.5 mol%) but different diameters, as presented in Figure 4c,d, it can be seen that D233 can produce higher power than D638. The increase was determined to be a factor of 3. This is

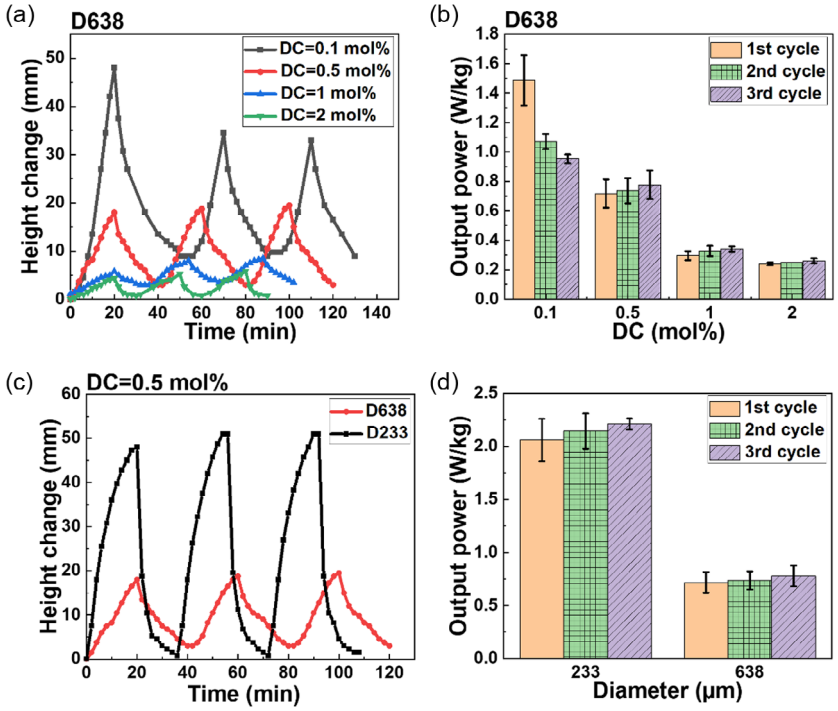

FIGURE 4 | (a) Height change of D638 particles with varied DC in engine 1.0 (see Figure 2b, syringe-type engine with a volume of 50 mL) in three consecutive cycles within a single experiment. (b) Output power of D638 particles as a function of DC (Particles with DC = 0.1 mol% are not chosen for further exploration due to their poor mechanical strength, as shown in Figure S1). (c) Height change of D233 and D638 particles (DC = 0.5 mol%) in engine 1.0 in three consecutive cycles within a single experiment. (d) Output power as a function of particle diameter (DC = 0.5 mol%) in engine 1.0 in three consecutive cycles. The error bars represent standard deviation from three independent experiments (n = 3).

most probably due to the shorter diffusion paths inside smaller particles, resulting in shorter diffusion time, as described by Fick's second law and in the simplest case as $\langle r^2 \rangle = 2nDt$, where r is the radius of the particle, n is the dimensionality, D is the self-diffusion coefficient of water ($D \approx 2 \times 10^{-9}$ m^2·s^{-1} at 25°C), and t is the time allowed for diffusion [61]. Based on this equation, water requires approximately 8.48 s to diffuse into D638 dry particles, whereas it takes only about 1.13 s for D233 dry particles, indicating a roughly 7.5-fold faster time scale.

2.5 | Power Generation via Engine 2.0

The influence of engine operating parameters on power production was investigated with engine 2.0. As smaller particles show better performance in power production in engine 1.0, D233 particles were further tested in engine 2.0. Measurements with engine 2.0 included four variable parameters, which were dry gel mass, cycle time, applied pressure, and flow rate. Those four operational parameters were optimized sequentially using a one-factor-at-a-time approach, with the goal of obtaining the maximum power.

First, the influence of dry gel mass on power production was explored, as shown in Figure 5a. The fixed parameters included a cycle time of 32 min, a pressure of 11 kPa, and a flow rate of 100 mL·min^{-1}. When the applied mass is too small, the hydrogels cannot fully cover the engine bottom after swelling in saline, leading to a delayed expansion, a longer cycle time, and consequently reduced power output. On the contrary, by application of a too large mass of hydrogels, gel-blocking will be more pronounced due to the more stacked layers. Under the influence of these two aspects, the power generation shows a slight trend of first increasing and then decreasing with masses ranging from 0.5 g to 2.0 g. Although the differences in power are relatively small, a dry gel mass of 1.5 g yielded the highest mean power output and was therefore selected for further experiments, yielding a dry mass-to-surface ratio of 191 g· m^{-2}, as shown in Table 2.

Second, the cycle time for power generation was tuned. Here, the dry gel mass was fixed at 1.5 g, the pressure was held at 11 kPa, and the flow rate was fixed at 100 mL·min^{-1}. The swelling behavior of the particles in DI water would exhibit a sigmoidal dependence on time if the time is long enough. The corresponding swelling rate (change of volume per time) initially increases rapidly, reaches a maximum, and then gradually decreases until barely changing. The deswelling has a similar time dependence, first the deswelling rate is high, then it declines. Its behavior is similar to the swelling, yet substantially faster due to the diffusion of salt ions inside hydrogels which reduces osmotic pressure immediately. As the applied cycle time also significantly affects the output power from the osmotic engine, the efficiency of the process can be increased by performing the swelling-deswelling cycle within shorter time. As shown in Figure 5b, the output power increases with shorter cycle times, and then decreases significantly at longer cycle times (e.g., 42 min). A cycle time of 7 min, including a swelling time of 4 min and a deswelling time of 3 min, was selected for further experiments as it yielded the highest mean power output within the investigated range. The disadvantage of shorter cycle times is the reduced penetration depth into the hydrogels, while the drawback of longer cycle times is a lower average expansion rate.

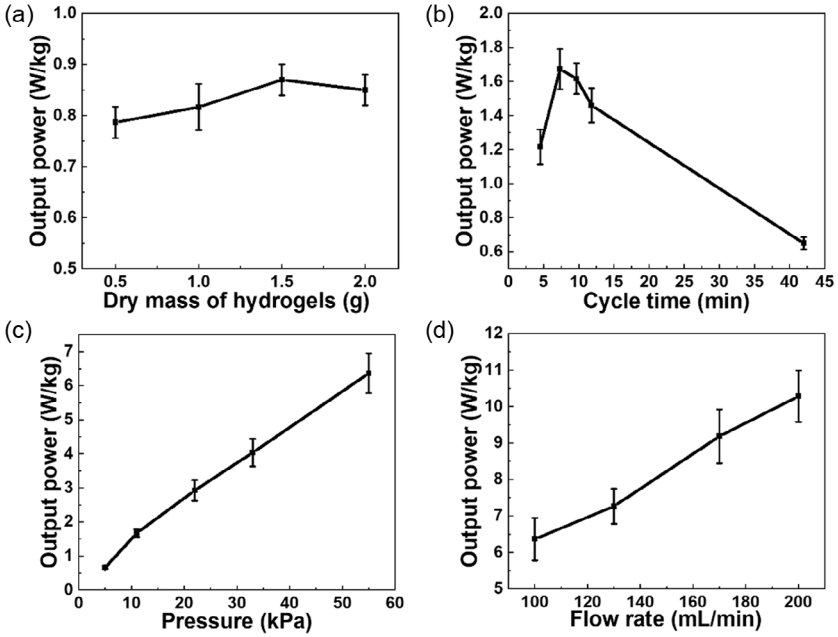

FIGURE 5 | Output power produced by D233 (DC = 0.5 mol%) in engine 2.0 (see Figure 2c, with a volume of 1 L) as a function of (a) dry gel mass (cycle time = 32 min, pressure = 11 kPa, flow rate = 100 mL·min^{-1}), (b) cycle time (dry gel mass = 1.5 g, pressure = 11 kPa, flow rate = 100 mL·min^{-1}), (c) pressure (dry gel mass = 1.5 g, cycle time = 7 min, flow rate = 100 mL·min^{-1}), and (d) flow rate (dry gel mass = 1.5 g, cycle time = 7 min, pressure = 55 kPa). All data points represent mean ± standard deviation from three independent experiments (n = 3).

TABLE 2 | Optimization of operation parameters on output power in engine 2.0 produced by D233 (DC = 0.5 mol%) particles. The standard deviation represents three independent experiments (n = 3).

Fixed parameters	Variable and optimum value	Mean output power ± standard deviation
Cycle time: 32 min Pressure: 11 kPa Flow rate: 100 mL·min^{-1}	Dry gel mass: 1.5 g	0.87 ± 0.03 W·kg^{-1}
Dry gel mass: 1.5 g Pressure: 11 kPa Flow rate: 100 mL·min^{-1}	Cycle time: 7 min	1.67 ± 0.12 W·kg^{-1}
Dry gel mass: 1.5 g Cycle time: 7 min Flow rate: 100 mL·min^{-1}	Pressure: 55 kPa	6.37 ± 0.59 W·kg^{-1}
Dry gel mass: 1.5 g Cycle time: 7 min Pressure: 55 kPa	Flow rate: 200 mL·min^{-1}	10.28 ± 0.71 W·kg^{-1}

Thirdly, the effect of the added load and therefore pressure on the hydrogel particles on power production was investigated. The constant parameters were a dry gel mass of 1.5 g, a cycle time of 7 min, and a flow rate of 100 mL·min^{-1}. As shown in Figure 5c, higher pressure leads to a higher power output (see Equation (1)). The pressure of 55 kPa is found to be the limit value for engine 2.0 due to the structural limitation (see Chapter 4.5). The microscope image of D233 after 10 consecutive swelling-shrinking cycles in engine 2.0 under 55 kPa (Figure S2) shows that most of the particles still keep the original spherical shapes without breakage or rupture. As a result, 55 kPa of pressure is regarded as the maximum possible value for this engine type (2.0) but not for the SAPs.

Finally, the applied flow rate was adjusted to reach the maximum power output. During this exploration other operating parameters were fixed as a dry gel mass of 1.5 g, a cycle time of 7 min, and a pressure of 55 kPa, which were the optimal values from previous tests, as mentioned above. With higher flow rates the transportation of liquid into the engine and out of the engine is faster, which is beneficial for removing the residual solution from the previous process and restoring the osmotic pressure difference. This increases the swelling rate and leads to a higher output power, as shown in Figure 5d. The practical limit for engine 2.0 was determined to be 200 mL·min^{-1} for the specific setup as with further increased flow rates (e.g. 400 mL·min^{-1}), the introduced pressure from the pumps will push up the particles from the engine bottom and hinder accurate height observation. The reason is that higher pressure causes greater particle deformation and stronger interparticle compression, reducing the voids between the particles, and thus leading to more severe gel-blocking. This retards liquid

transport, and the residual liquid exerts an upward force on the gel. Therefore, the flow rate for power generation is kept at the highest possible value for this engine, which is a constant flux of 200 mL·min^{-1}.

Table 2 lists the achieved output power after each optimization step for engine 2.0 with D233 particles. The height change with each parameter can be found in Figure S3. However, the one-factor-at-a-time approach we used here might not reach the maximum power as it doesn't account for possible interactions among parameters, while in practice the optimum cycle time will change with higher flow rate and pressure. Therefore, further experiments were carried out to explore the influence of cycle time with a dry gel mass of 1.5 g, an applied pressure of 55 kPa and a flow rate of 200 mL·min^{-1}. The details of exploring the optimum cycle time are as follows: firstly, the full curve of swelling and deswelling until reaching equilibrium was recorded, as shown in Figure 6a with a cycle time of 23 min. The experimentally observed swelling and deswelling kinetics were described using phenomenological Equations (5) and (6). During the experiment the gels were placed in contact and subjected to external pressure, resulting in mechanical confinement and mutual deformation compared to free diffusion. Such conditions make the classical analytical solutions to Fick's second law of diffusion not strictly applicable [62]. The unit for the prefactor 26.24 (amplitude of change) is in mm and the unit for t is in s. The onset of the deswelling phase t_0 is 600 s in this situation. The swelling rate constant (5.83×10^{-3}) is smaller than the deswelling rate constant (0.01), indicating that the swelling process proceeds slower than the contraction process.

$$y_{\text{swell}} = 26.24 \times (1 - \exp(-(5.83 \times 10^{-3} \times t)^{1.40})) \text{ [mm]} \quad (5)$$

$$y_{\text{deswell}} = 26.24 \times \exp(-(0.01 \times (t - t_0))^{0.59}) \text{ [mm]} \quad (6)$$

From the height change rate of the cycle time of 23 min, as shown in Figure 6b, the fastest expansion rate is found to occur at 1.12 min, corresponding to the height of 6.20 mm. It is assumed that if the swelling cycle is started symmetrically around this point and deswelling follows as soon as possible, the output power can be increased remarkably due to the reduction of cycle time. Therefore, the shorter cycle time was controlled as follows: in the first cycle hydrogels were swollen to equilibrium in DI water until no height change was observed, and the deswelling in saline of this cycle was interrupted once the sample reached the height of the start point (6.20 mm). Then the second cycle was started at this point with the expansion time as a variable, as shown in the video S1 (played at 100× speed). Predicted output power using the respective swelling time as a variable was calculated through Equations (5) and (6), as shown in Table 3. Then practical experiments were carried out to confirm the predictions, as shown in Figure 6a. Both predicted and experimental output power values (see Table 3) show the behavior of first increasing and then decreasing with increasing cycle times. However, the experimental optimum cycle time is determined to be 7 min rather than 5.57 min as from the predicted value. The slight deviation can be explained by an expansion delay due to unfinished shrinkage in shortened time cycles and a swelling latency associated with the change of liquid feed. As shown in Figure 6c, a maximum output power of 13.20 ± 0.85 W·kg^{-1} is obtained with 7 min as cycle time, including a swelling time of 4 min and a deswelling time of 3 min. This optimum cycle time is consistent with the result from Figure 5b, but the start height of shorter cycles is lower due to the larger slope of swelling curve with higher flow rate, which leads to a higher power output.

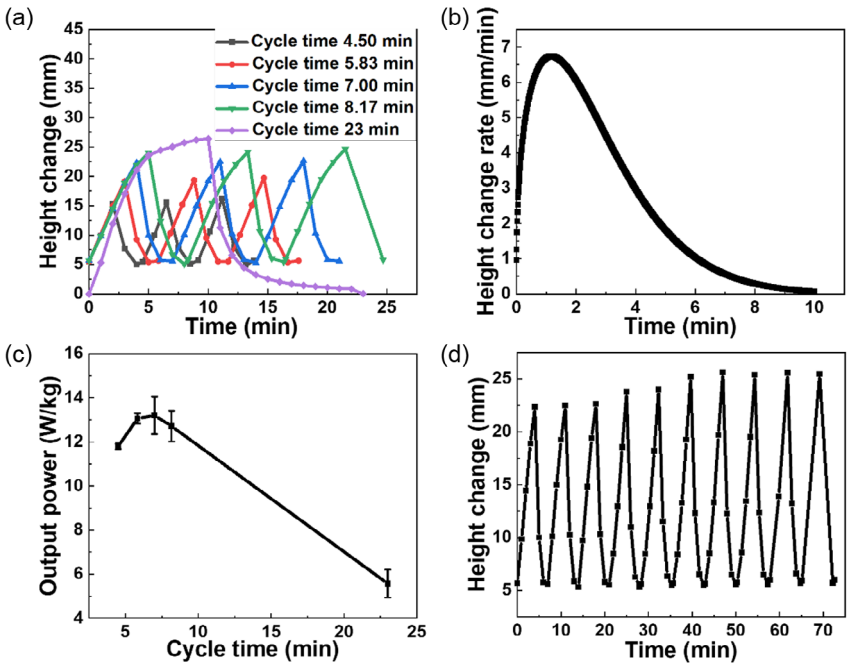

FIGURE 6 | (a) Height change of D233 particles (DC = 0.5 mol%) in engine 2.0 with varied cycle time and fixed parameters of a dry gel mass of 1.5 g, a pressure of 55 kPa and a flow rate of 200 mL·min^{-1}. (b) The height change rate of D233 hydrogels operating in a cycle time of 23 min. (c) Output power produced by D233 in engine 2.0 with varied cycle time and fixed parameters of a dry gel mass of 1.5 g, a pressure of 55 kPa and a flow rate of 200 mL·min^{-1}. Error bars represent standard deviation from three independent experiments (n = 3). (d) Height change of D233 in 10 cycles within a single experiment with fixed parameters of a cycle time of 7 min, a dry gel mass of 1.5 g, a pressure of 55 kPa and a flow rate of 200 mL·min^{-1}.

TABLE 3 | Predicted and experimental output power with varied cycle time using D233 particles in engine 2.0. The standard deviation represents three independent experiments ($n = 3$).

Swelling time (min)	Predicted cycle time (min)	Predicted output power ($W \cdot kg^{-1}$)	Experimental cycle time (min)	Experimental output power ± standard deviation ($W \cdot kg^{-1}$)
2	4.39	14.80	4.50	11.80 ± 0.12
3	5.57	15.32	5.83	13.06 ± 0.24
4	6.64	14.79	7.00	13.20 ± 0.85
5	7.66	13.81	8.17	12.71 ± 0.70
10	—	—	23.00	5.58 ± 0.63

Figure 6d shows the height change of D233 particles in 10 cycles with 7 min cycle time, which confirms the reusability of the hydrogels.

Through optimizing the operating parameters with D233 in engine 2.0, an output power of 13.20 ± 0.85 $W \cdot kg^{-1}$ was generated, which is around 6 times higher than in engine 1.0 with the same sample. This power also significantly exceeds the values reported for previously developed hydrogel-based osmotic engines, which range from 0.1 to 3.7 $W \cdot kg^{-1}$ [23, 37, 39, 40, 44]. This enhancement is primarily attributed to the redesigned engine with a reduced height-to-diameter ratio and the systematic optimization of operating parameters, which effectively alleviates gel-blocking and ensures sufficient water transportation. These results demonstrate that, in addition to hydrogel material development, engine architecture design and process optimization are also critical for unlocking the potential of salinity-gradient energy conversion.

3 | Conclusion

In this work, superabsorbent polymers were investigated in two types of osmotic engines with different volumes and height-to-diameter ratios to generate power through a salinity gradient. Polyacrylic acid hydrogel particles with mean diameters of $D = 233$ µm (abbreviated: D233) and $D = 638$ µm (abbreviated: D638) were synthesized with a flow-focusing microfluidic device. First, D638 hydrogel particles with different degree of crosslinking (DC) were tested in engine 1.0 (a syringe-type engine of 50 mL). It was found that DC = 0.5 mol% was the optimum value in a prediction via a figure of merit. This figure of merit was based on the difference of the products of Young's modulus and absorbency between deionized water and 43 $g \cdot L^{-1}$ NaCl solution, and the prediction was consistent with the experimental observations. By comparing the power of hydrogel particles with two different diameters in engine 1.0, it was found that D233 particles could generate about 3 times higher power than D638 particles due to the shorter diffusion time of the solution into the particles. Therefore, D233 particles were further investigated in engine 2.0 with an internal volume of 1 L. After optimization of the operation parameters, the optimal conditions of this setup were determined to be a dry gel mass of 1.5 g, a pressure of 55 kPa, a flow rate of 200 $mL \cdot min^{-1}$ and a cycle time of 7 min. With these parameters a maximum output power of 13.20 $W \cdot kg^{-1}$ dry superabsorber was obtained through operating engine 2.0 in deionized water and 43 $g \cdot L^{-1}$ NaCl solution. The results demonstrate the potential of microfluidic-synthesized hydrogel particles as scalable and controllable osmotic matrix materials and highlight that rational engine design and operating parameter optimization offer a viable pathway toward practical salinity-gradient energy harvesting.

Based on the results demonstrated in this work, several promising directions for future research can be identified. First, further reduction of particle size could enhance swelling kinetics and power output. Alternative synthesis methods such as suspension polymerization may enable the scalable production of smaller particles beyond the limitations of the current microfluidic setup. Second, the development of cationic or zwitterionic hydrogels could extend the applicability of osmotic engines to real seawater environments, where divalent cations would not affect the swelling performance as they do in anionic PAA hydrogels.

4 | Experimental Section

4.1 | Materials

Acrylic acid (AA, 98%), 2,2′-azobis(2-methylpropionamidine) dihydrochloride (V50), and mineral oil (petroleum, spectroscopy grade) were purchased from Thermo Fisher Scientific and used without further purification, N,N′-methylenebisacrylamide (MBA) was purchased from Sigma Aldrich. Sodium hydroxide (NaOH) was supplied by Carl Roth. The surfactant ABIL EM 90 (nonionic water/oil emulsifier with a polymeric structure based on silicone; viscosity, η = 1–2.3 Pa·s @ 25°C) was supplied from Evonik Industries.

4.2 | Synthetic Procedure Using a Flow-Focusing Microfluidic Device

The self-built microfluidic device (Figure 1a) was made of two capillary tubes, a round one with inner diameter of 0.58 or 1.4 mm and a square one with width of 1.1 or 2.2 mm. The round capillary was partially inserted into the squared capillary and they were fixed on a glass microscope slide with transparent epoxy glue and connected to two needle tips that served as inlets for the water and oil phases. One needle was attached on the tip of the square capillary and another one was placed on the intersection of the two capillaries. Two syringe pumps (Harvard Apparatus, PHD Ultra) were used to control the flow rates of the water phase and the oil phase from disposable syringes (BD Pastipak) into the flow-focusing device.

The oil phase consisted of mineral oil containing 10 wt% of surfactant ABIL EM 90, and the water phase included the reactive mixture of monomer AA neutralized by NaOH, crosslinker MBA, DI water, and photo-initiator V50.

The synthesis of the hydrogel particles with a diameter of 638 μm, DC = 0.5 mol% and DN = 75 mol% is given here as an example. First, MBA (0.04 g, 0.25 mmol) was dissolved in DI water (9.85 g). Subsequently, AA (3.60 g, 50.0 mmol) was added and the mixture was cooled in an ice bath. Then, 33 wt% NaOH-solution (4.55 g, 37.5 mmol) was added dropwise to the mixture for neutralization. After purging the solution with nitrogen for 15 min, V50 (0.02 g, 0.06 mmol) dissolved in DI water (1 g) was added. For the oil phase, 54 g of mineral oil and 6 g of ABIL EM 90 were mixed until homogenous. The solutions were taken up into respective syringes and used for microfluidic synthesis in a device with capillaries of inner diameters of 1.4 mm (round) and 2.2 mm (square), using flow rates of 17 $mL \cdot h^{-1}$ and 60 $mL \cdot h^{-1}$ for the water and oil phase, respectively. The obtained droplets were polymerized under UV light (100 W longwave mercury spot lamp) for 2 h and left to cure overnight. The resulting particles were washed 3 times with isopropanol, 3 times with DI water, and dried at 70°C under reduced pressure of 100 mbar for 2 days.

4.3 | Absorbency Measurements

The equilibrium degrees of swelling in deionized water (Q_{DI}) and saline water (Q_S) were measured gravimetrically. To do so, 0.1 g of dry particles (m_{dry}) were completely immersed in 50 mL saline (43 $g \cdot L^{-1}$ NaCl solution, which has similar ionic strength as seawater [39]) for 24 h. Then they were filtered through a metal sieve with a mesh size of 600 μm to remove surplus saline solution. After measuring the particle mass, the absorbency in saline could be calculated. The hydrogels swollen in saline solution were then transferred into 100 mL DI water, and after 24 h and removal of the supernatant the mass of particles in DI water was obtained, and the absorbency in DI water could be calculated. All experiments were repeated 3 times and the results are reported as mean ± standard deviation (n = 3 independent experiments).

4.4 | Rheological Characterization

The mechanical properties of hydrogels were studied by oscillatory shear experiments performed on a strain-controlled rheometer ARES G2 (TA Instruments, Eschborn, Germany). The test geometry was a 25 mm parallel plate–plate geometry made from stainless steel. Measurements were performed at a temperature of 20°C which was controlled by a Peltier element (Advanced Peltier System, TA Instruments) under a constant pressure (normal force) of 4 kPa. The lower geometry consisted of a cup with a diameter of 25 mm, whose rim of 1 mm was intended to prevent the particles from escaping, as shown in Figure S4. For each sample, first an oscillatory strain sweep ranging from $\gamma_0 = 10^{-5}$ to 0.1 was recorded at a constant angular frequency (ω = 1 $rad \cdot s^{-1}$) to determine the linear viscoelastic regime. Then an angular frequency sweep (ω = 0.1–100 $rad \cdot s^{-1}$) was performed at a constant strain amplitude of $\gamma_0 = 0.1\%$. As the hydrogels are mostly elastic, the mean value of the storage modulus (G') at an angular frequency of 1 $rad \cdot s^{-1}$ was considered to be representative for $|G^*|$ of the sample. The error bars in the respective graphs indicate the standard deviation around the mean value from 3 independent repeated measurements.

4.5 | Osmotic Engine Performance Measurements

4.5.1 | Engine 1.0

This is a syringe-type engine with a volume of 50 mL. There is one inlet at the bottom, which is connected to the pipes to pump in the feed liquids. The excess can be drawn out though the four holes on the piston with another pump (peristaltic pump LA-900, Landgrave HLL). Before starting the experiment, dried hydrogels of 0.2 g with varied DC were swollen to equilibrium in saline solution. The swollen particles were then placed between two filter papers (mesh size 3–5 μm) and two metal wires (mesh size 120 μm) to prevent particles from escaping the setup. A weight of 2 kg was put on top of the piston and this resulted in a pressure of 28 kPa due to the surface area of 7.07 cm^2 (diameter 3 cm). First, DI water was pumped into the engine to induce the swelling of the hydrogels and push the piston up. The swelling period was 20 min and during this time, the height of the piston was recorded every 2 min. Then, the inlet flow was changed to saline until the hydrogels were deswelling to a constant volume. The flow rate was kept at 10 $mL \cdot min^{-1}$.

4.5.2 | Engine 2.0

It contains separate inlets for saline and DI water, which simplifies the operation of the engine. Furthermore, liquid can be extracted from the piston hole through another tube. The masses of particles were varied and placed inside the engine between two filter papers (mesh size 3–5 μm) and two metal gauzes (mesh size 120 μm). The weights on the piston were 4.5, 10.1, 14.6, 20.4, 30.5, and 50.3 kg, which corresponded to the pressures of 5, 11, 16, 22, 33, and 55 kPa due to the surface area of 91.56 cm^2 (diameter 10.80 cm). The height change was recorded by a distance gauge (MarCator 1086, Mahr, Göttingen, Germany) every 2 min, as shown in Video S1. The pressure of 55 kPa is found to be the limit value for engine 2.0 as higher pressure will cause fluid leaking at the engine connections, which can damage the engine in the long run. It is thus not an intrinsic limit of engine 2.0; rather it is the highest pressure safely testable in the current set-up. Possible mitigation routes would enable higher test pressures, such as reinforcing fittings and employing stronger materials like metal. All experiments were repeated 3 times and the results are reported as mean ± standard deviation (n = 3 independent experiments).

Acknowledgments

The authors acknowledge the financial support from Chinese Scholarship Council (CSC) and German Research Foundation (DFG 1911/24-2). The authors are grateful to the mechanical workshop of ITCP and Mr. Daniel Zimmermann for the engine constructions. The authors thank former group members, Dr. Lukas Arens, Dr. Amir Jangizehi, and Dr. Christian Fengler for the previous exploration on microfluidic synthesis and osmotic engines.

Open Access funding enabled and organized by Projekt DEAL.

Funding

This study was supported by German Research Foundation (DFG 1911/24-2) and Chinese Scholarship Council (CSC).

Conflicts of Interest

The authors declare no conflicts of interest.

Data Availability Statement

The data that support the findings of this study are available from the corresponding author upon reasonable request.

References

1. R. A. Tufa, S. Pawlowski, J. Veerman, et al., "Progress and Prospects in Reverse Electrodialysis for Salinity Gradient Energy Conversion and Storage," *Applied Energy* 225 (2018): 290.

2. S. Chu and A. Majumdar, "Opportunities and Challenges for a Sustainable Energy Future," *Nature* 488 (2012): 294.

3. R. Lee, "The Outlook for Population Growth," *Science* 333 (2011): 569.

4. A. Gałecka and M. Pyra, "Changes in the Global Structure of Energy Consumption and the Energy Transition Process," *Energies* 17 (2024): 5644.

5. Y. Zhao, M. Li, R. Long, Z. Liu, and W. Liu, "Review of Osmotic Heat Engines for Low-Grade Heat Harvesting," *Desalination* 527 (2022): 115571.

6. M.-Y. Yu, J. Wu, G. Yin, F.-Z. Jiao, Z.-Z. Yu, and J. Qu, "Dynamic Regulation of Hydrogen Bonding Networks and Solvation Structures for Synergistic Solar-Thermal Desalination of Seawater and Catalytic Degradation of Organic Pollutants," *Nano-Micro Letters* 17 (2024): 48.

7. C. Seyfried, H. Palko, and L. Dubbs, "Potential Local Environmental Impacts of Salinity Gradient Energy: A Review," *Renewable and Sustainable Energy Reviews* 102 (2019): 111.

8. M. Khayet, E. Aytaç, M. Essalhi, et al., "Elucidating the Dynamics of Salinity Gradient Energy Research," *Renewable and Sustainable Energy Reviews* 219 (2025): 115812.

9. K. L. Lee, R. W. Baker, and H. K. Lonsdale, "Membranes for Power-Generation by Pressure-Retarded Osmosis," *Journal of Membrane Science* 8 (1981): 141.

10. R. E. Pattle, "Production of Electric Power by Mixing Fresh and Salt Water in the Hydroelectric Pile," *Nature* 174 (1954): 660.

11. S. Loeb and R. S. Norman, "Osmotic Power Plants," *Science* 189 (1975): 654.

12. G. M. Zentner, G. S. Rork, and K. J. Himmelstein, "The Controlled Porosity Osmotic Pump," *Journal of Controlled Release* 1 (1985): 269.

13. Q. Zheng, Y. Shen, L. Wang, et al., "Clay-Based Nanofluidic Membrane with Enhanced Space Charge for Robust Osmotic Energy Harvesting," *ACS Applied Materials & Interfaces* 17 (2025): 29469.

14. S. Lin, A. P. Straub, and M. Elimelech, "Thermodynamic Limits of Extractable Energy by Pressure Retarded Osmosis," *Energy & Environmental Science* 7 (2014): 2706.

15. N. Voutchkov, "Energy Use for Membrane Seawater Desalination – Current Status and Trends," *Desalination* 431 (2018): 2.

16. M. M. Rahman, "Membranes for Osmotic Power Generation by Reverse Electrodialysis," *Membranes* 13 (2023): 164.

17. S. Zhang, S. Lin, X. Zhao, and R. Karnik, "Thermodynamic Analysis and Material Design to Enhance Chemo-Mechanical Coupling in Hydrogels for Energy Harvesting from Salinity Gradients," *Journal of Applied Physics* 128 (2020): 044701.

18. Y. Liu, J. Song, Z. Liu, et al., "Anti-Swelling Polyelectrolyte Hydrogel with Submillimeter Lateral Confinement for Osmotic Energy Conversion," *Nano-Micro Letters* 17 (2024): 81.

19. S. Lin, Z. Wang, L. Wang, and M. Elimelech, "Salinity Gradient Energy Is Not a Competitive Source of Renewable Energy," *Joule* 8 (2024): 334.

20. X. Zhu, W. Yang, M. C. Hatzell, and B. E. Logan, "Energy Recovery from Solutions with Different Salinities Based on Swelling and Shrinking of Hydrogels," *Environmental Science & Technology* 48 (2014): 7157–7163.

21. T. Q. Bui, V. D. Cao, N. B. D. Do, et al., "Salinity Gradient Energy from Expansion and Contraction of Poly(allylamine Hydrochloride) Hydrogels," *ACS Applied Materials & Interfaces* 10 (2018): 22218.

22. Y. Huang, P. Shen, Q. Ma, et al., "A General Approach of Reinforcing Hydrogels for Salinity-Gradient Energy Harvesting," *Nano Energy* 138 (2025): 110898.

23. T. Q. Bui, V. D. Cao, W. Wang, and A. L. Kjoniksen, "Recovered Energy from Salinity Gradients Utilizing Various Poly(Acrylic Acid)-Based Hydrogels," *Polymers* 13 (2021): 645.

24. X. Zhu, P. Qi, W. Fan, H. Wang, and K. Sui, "Bioinspired Multifunctional Self-Powered Ionic Receptors Derived by Gradient Polyelectrolyte Hydrogels," *Chemical Engineering Journal* 438 (2022): 135610.

25. D. Li, X. Zhang, G. P. Simon, and H. Wang, "Forward Osmosis Desalination Using Polymer Hydrogels as a Draw Agent: Influence of Draw Agent, Feed Solution and Membrane on Process Performance," *Water Research* 47 (2013): 209.

26. Z. Li, Y. Zhou, T. Qin, et al., "Global Research and Emerging Trend of Superabsorbent Hydrogel Applied to Agriculture Based on Visual Analysis," *Water, Air, & Soil Pollution* 236 (2025): 359.

27. E. Tabesh, D. Grumme, M. Herb, et al., "Fabrication of MXene Integrated Superabsorbent Polymers Composites Hydrogels for Bacterial Enrichment," *Separation and Purification Technology* 368 (2025): 133022.

28. A. Katchalsky and I. Michaeli, "Polyelectrolyte Gels in Salt Solutions," *Journal of Polymer Science* 15 (1955): 69.

29. X. He, J. Zhu, and C. Yang, "Harnessing Osmotic Swelling Stress for Robust Hydrogel Actuators," *Soft Matter* 18 (2022): 5177.

30. D. Li, X. Zhang, J. Yao, G. P. Simon, and H. Wang, "Stimuli-Responsive Polymer Hydrogels as a New Class of Draw Agent for Forward Osmosis Desalination," *Chemical Communications* 47 (1710): 2011.

31. Y. Liu, J. Li, S. Huang, et al., "Synthesis, Characterization, and Application of Biodegradable Superabsorbent Gels Based on Carboxymethyl Chitosan-Modified Sodium Lignosulfonate," *European Polymer Journal* 230 (2025): 113905.

32. X. Le, W. Lu, J. Zhang, and T. Chen, "Recent Progress in Biomimetic Anisotropic Hydrogel Actuators," *Advanced Science* 6 (2019): 1801584.

33. B. Somchob, N. Passornraprasit, V. P. Hoven, and N. Rodthongkum, "Dual-Crosslinked Zwitterionic Hydrogel: A Facile Platform of Wearable Colorimetric Urea Sensors," *Mikrochimica Acta* 192 (2025): 204.

34. P. J. Flory and J. Rehner, "Statistical Mechanics of Cross-Linked Polymer Networks I. Rubberlike Elasticity," *The Journal of Chemical Physics* 11 (1943): 512.

35. N. A. Neuburger and B. E. Eichinger, "Critical Experimental Test of the Flory-Rehner Theory of Swelling," *Macromolecules* 21 (1988): 3060.

36. X. Pan, Q. Wang, D. Benetti, Y. Ni, and F. Rosei, "Polyelectrolyte Hydrogel: A Versatile Platform for Mechanical-Electric Conversion and Self-Powered Sensing," *Nano Energy* 103 (2022): 107718.

37. A. C. Padmanabhan, D. S. Han, S. Zavahir, J. Tkac, and P. Kasak, "Tandem Osmotic Engine Based on Hydrogel Particles with Antipolyelectrolyte and Polyelectrolyte Effect Fuelled by Both Salinity Gradient Modes," *Gels* 7 (2021): 232.

38. H. Choudhary and S. R. Raghavan, "Superfast-Expanding Porous Hydrogels: Pushing New Frontiers in Converting Chemical Potential into Useful Mechanical Work," *ACS Applied Materials & Interfaces* 14 (2022): 13733.

39. A. Jangizehi, C. Fengler, L. Arens, and M. Wilhelm, "Optimizing the Power Production in an Osmotic Engine via Microfluidic Fabricated and Surface Crosslinked Hydrogels Utilizing Fresh and Salt Water," *Macromolecular Materials and Engineering*, 305 (2020): 2000174.

40. L. Arens, F. Weissenfeld, C. O. Klein, K. Schlag, and M. Wilhelm, "Osmotic Engine: Translating Osmotic Pressure into Macroscopic Mechanical Force via Poly(Acrylic Acid) Based Hydrogels," *Advanced Science* 4 (2017): 1700112.

41. T. C. Hales, "The Sphere Packing Problem," *Journal of Computational and Applied Mathematics* 44 (1992): 41.

42. D. K. Hwang, D. Dendukuri, and P. S. Doyle, "Microfluidic-Based Synthesis of Non-Spherical Magnetic Hydrogel Microparticles," *Lab on a Chip* 8 (1640): 2008.

43. H. Wack and M. Ulbricht, "Effect of Synthesis Composition on the Swelling Pressure of Polymeric Hydrogels," *Polymer* 50 (2009): 2075.

44. Y. Hong, Y. Wang, Y. Tian, Z. Wang, C. Hu, and J. Ma, "Extracting Salinity Gradient Energy via Antifouling Poly(acrylic Acid-Co-Acrylamide) Hydrogels in Natural Water," *ACS Applied Polymer Materials* 3 (2021): 6513.

45. D. Zhao, L. Qian, Q. Yang, et al., "Microfluidic Synthesis of Stimuli-Responsive Hydrogel Particles," *Applied Materials Today* 42 (2025): 102571.

46. H. Fallahi, J. Zhang, H. P. Phan, and N. T. Nguyen, "Flexible Microfluidics: Fundamentals, Recent Developments, and Applications," *Micromachines* 10 (2019): 830.

47. S. Zeng, X. Liu, H. Xie, and B. Lin, "Basic Technologies for Droplet Microfluidics," in*Microfluidics: Technologies and Applications*, ed.B. Lin (Springer, 2011), 69.

48. C. Martino and A. J. deMello, "Droplet-Based Microfluidics for Artificial Cell Generation: A Brief Review," *Interface Focus* 6 (2016): 20160011.

49. M. Chen, G. Bolognesi, and G. T. Vladisavljevic, "Crosslinking Strategies for the Microfluidic Production of Microgels," *Molecules* 26 (2021): 3752.

50. X. Zhang, Q. Qu, A. Zhou, et al., "Core-Shell Microparticles: From Rational Engineering to Diverse Applications," *Advances in Colloid and Interface Science* 299 (2022): 102568.

51. W. Zheng, R. Xie, X. Liang, and Q. Liang, "Fabrication of Biomaterials and Biostructures Based on Microfluidic Manipulation," *Small* 18 (2022): e2105867.

52. C. Fengler, L. Arens, H. Horn, and M. Wilhelm, "Desalination of Seawater Using Cationic Poly(acrylamide) Hydrogels and Mechanical Forces for Separation," *Macromolecular Materials and Engineering* 305 (2020): 2000383.

53. K. K. Phani and D. Sanyal, "The Relations between the Shear Modulus, the Bulk Modulus and Young's Modulus for Porous Isotropic Ceramic Materials," *Materials Science and Engineering: A* 490 (2008): 305.

54. R. G. Larson, *The Structure and Rheology of Complex Fluids* (Oxford University Press, 1999).

55. R. J. Young and P. A. Lovell, *Introduction to Polymers*, 3rd ed.(CRC Press, 2011).

56. M. M. Villone and P. L. Maffettone, "Dynamics, Rheology, and Applications of Elastic Deformable Particle Suspensions: A Review," *Rheologica Acta* 58 (2019): 109.

57. H. M. Shewan, G. E. Yakubov, M. R. Bonilla, and J. R. Stokes, "Viscoelasticity of Non-Colloidal Hydrogel Particle Suspensions at the Liquid–Solid Transition," *Soft Matter* 17 (2021): 5073.

58. X. Zhao, "Multi-Scale Multi-Mechanism Design of Tough Hydrogels: Building Dissipation into Stretchy Networks," *Soft Matter* 10 (2014): 672.

59. J. P. Gong, "Why Are Double Network Hydrogels So Tough?," *Soft Matter* 6 (2010): 2583.

60. M. Doi and S. F. Edwards, *The Theory of Polymer Dynamics* (Clarendon Press, 1986).

61. L. Simon and J. Ospina, "On the Effusion Time of Drugs from the Open Pore of a Spherical Vesicle," *Physica A: Statistical Mechanics and Its Applications* 451 (2016): 366.

62. J. Crank, *The Mathematics of Diffusion*, 2nd ed. (Clarendon Press, 1975).

Supporting Information

Additional supporting information can be found online in the Supporting Information section.